Membrane perforation by the pore-forming toxin pneumolysin

Membrane perforation by the pore-forming toxin pneumolysin

Martin Vögele[a], Ramachandra M. Bhaskara[a], Estefania Mulvihill[b], Katharina van Pee[c], Özkan Yildiz[c], Werner Kühlbrandt[c], Daniel J. Müller[b], and Gerhard Hummer[a,d,1]

[a]Department of Theoretical Biophysics, Max Planck Institute of Biophysics, 60438 Frankfurt am Main, Germany; [b]Department of Biosystems Science and Engineering, ETH Zürich, 4058 Basel, Switzerland; [c]Department of Structural Biology, Max Planck Institute of Biophysics, 60438 Frankfurt am Main, Germany; and [d]Institute for Biophysics, Goethe University Frankfurt, 60438 Frankfurt am Main, Germany

Edited by Michael L. Klein, Institute of Computational Molecular Science, Temple University, Philadelphia, PA, and approved May 21, 2019 (received for review March 12, 2019)

Pneumolysin (PLY), a major virulence factor of *Streptococcus pneumoniae*, perforates cholesterol-rich lipid membranes. PLY protomers oligomerize as rings on the membrane and then undergo a structural transition that triggers the formation of membrane pores. Structures of PLY rings in prepore and pore conformations define the beginning and end of this transition, but the detailed mechanism of pore formation remains unclear. With atomistic and coarse-grained molecular dynamics simulations, we resolve key steps during PLY pore formation. Our simulations confirm critical PLY membrane-binding sites identified previously by mutagenesis. The transmembrane β-hairpins of the PLY pore conformation are stable only for oligomers, forming a curtain-like membrane-spanning β-sheet. Its hydrophilic inner face draws water into the protein–lipid interface, forcing lipids to recede. For PLY rings, this zone of lipid clearance expands into a cylindrical membrane pore. The lipid plug caught inside the PLY ring can escape by lipid efflux via the lower leaflet. If this path is too slow or blocked, the pore opens by membrane buckling, driven by the line tension acting on the detached rim of the lipid plug. Interestingly, PLY rings are just wide enough for the plug to buckle spontaneously in mammalian membranes. In a survey of electron cryo-microscopy (cryo-EM) and atomic force microscopy images, we identify key intermediates along both the efflux and buckling pathways to pore formation, as seen in the simulations.

pore-forming toxin | cholesterol-dependent cytolysin | pneumolysin | membrane pore

Pneumolysin (PLY) is the most important virulence factor of the human pathogen *Streptococcus pneumoniae* (1). PLY is a β-pore–forming toxin (β-PFT) from the cholesterol-dependent cytolysin (CDC) family (2–4). *S. pneumoniae* attacks mammalian cells by releasing PLY in a water-soluble monomeric form (3, 5). The PLY protomers adhere to cholesterol-rich membranes and organize into closed rings, forming a prepore membrane protein complex (6–9). In an extensive structural transition, two helix bundles (HB1 and HB2) of the PLY protomers refold into β-hairpins and insert into the membrane to form a large oligomeric β-barrel (10). Perforation of the plasma membrane eventually leads to cell death by cytolysis (10). At sublytic concentrations, PLY exhibits toxic effects related to calcium influx (11, 12).

Three-dimensional structures of CDCs provide insights into their cytolytic activity. Crystal structures of PLY protomers (13–15) show that the soluble monomer is elongated and consists of four domains (D1–D4; Fig. 1, *Left*). The Trp-rich undecapeptide and loops L1–L3 on opposite sides of D4 are essential for membrane docking and anchoring. L1 residues (Thr459/Leu460) act as the main cholesterol-recognition motif (16) and determine the membrane selectivity of PLY. Oligomerization of membrane-bound protomers and the formation of PLY rings with cyclic symmetry are mediated by conserved surface residues with complementary shape and charge at the interface (13, 14), as also shown for listeriolysin-O (LLO) (17). A likely pathway of pore formation has emerged from intermediates captured by atomic force microscopy (AFM) and electron cryo-microscopy (cryo-EM) (15, 18, 19). After membrane binding and ring formation, the protomers transition through early and late prepore intermediates to the membrane-inserted pore state. In this transition, the two helix bundles HB1 and HB2 of D3 are brought close to the membrane by a hinge motion (15, 19). The transition is associated with a 4-nm contraction relative to the membrane surface, as observed in AFM experiments (15), the unfolding of the helix bundles, and their refolding as membrane-inserted β-hairpins HP1 and HP2.

The formation of the membrane-inserted β-sheets, the restructuring of the lipid membrane, and the formation of the pore are difficult to observe experimentally. Molecular dynamics (MD) simulations offer a promising alternative to resolve pore formation at the molecular scale. Previous MD simulations of α- and β-PFTs (20–25) were limited to either protein monomers or small oligomers. Simple rate models for the assembly and insertion process have been proposed (26, 27), but the role of lipids and the process of pore opening have not been studied in detail.

We use atomistic and coarse-grained MD simulations to study the binding of PLY to cholesterol-rich membranes, the organization of lipids around the prepore and pore conformations of PLY, and the formation of membrane pores. Water

Significance

Pneumolysin, a pore-forming toxin of *Streptococcus pneumoniae*, assembles into rings on cholesterol-containing membranes of host cells. β-hairpins form a barrel-shaped transmembrane β-sheet that perforates the membrane, leading to cell lysis. In atomistic and coarse-grained molecular dynamics simulations, we resolve how pneumolysin docks to cholesterol-rich bilayers and how membrane pores form. Remarkably, pneumolysin rings are just wide enough that pores form even if lipid efflux is blocked, driven by spontaneous buckling of the lipid plug. In a survey of electron microscopy and atomic force microscopy images, we identify key intermediates along both the lipid-efflux and plug-buckling pathways of pore opening.

Author contributions: Ö.Y., W.K., D.J.M., and G.H. designed research; M.V., R.M.B., E.M., and K.v.P. performed research; M.V., R.M.B., E.M., K.v.P., Ö.Y., W.K., D.J.M., and G.H. analyzed data; and M.V., R.M.B., and G.H. wrote the paper.

The authors declare no conflict of interest.

This article is a PNAS Direct Submission.

[1]To whom correspondence may be addressed. Email: gerhard.hummer@biophys.mpg.de.

This article contains supporting information online at www.pnas.org/lookup/suppl/doi:10.1073/pnas.1904304116/-/DCSupplemental.

Published online June 17, 2019.

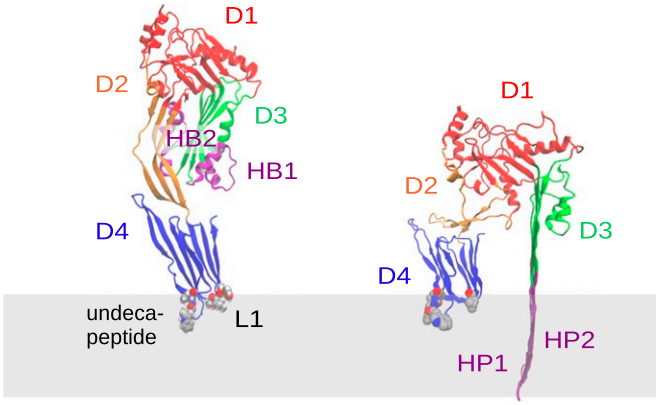

Fig. 1. Prepore (*Left*; X-ray structure, 5CR6) and pore (*Right*; cryo-EM structure, 5LY6) conformations of PLY protomer represent the starting and end states along the pore-formation process. The undecapeptide with the tryptophan residues Trp433, Trp435, and Trp436 and loop 1 (L1) with Thr459, Leu460, and Tyr461 (spheres) anchor PLY domain 4 (D4) to the membrane. Helix bundles HB1 and HB2 of domain 3 (D3) change their secondary structure and insert into the bilayer, forming transmembrane β-hairpins HP1 and HP2 (purple) in the pore conformation. The membrane is shown schematically as a gray band.

influx and the depletion of lipids from the inner rim of PLY oligomers emerge as the key steps. In simulations of membrane-bound PLY rings, we observe the removal of the lipid plug from the PLY ring. We validate our pore-opening simulations by comparing key intermediates to earlier AFM and EM images. Application of membrane elastic theory to the lipid patch enclosed by the PLY ring supports our simulation results and explains the size dependence of pore formation.

Results

Membrane Interactions of Pneumolysin. In the prepore conformation, PLY interacts with membranes via the undecapeptide and loop 1 (L1) of D4. To characterize the membrane interaction of PLY and account for its cholesterol dependence, we performed all-atom MD simulations of PLY monomers adhered via D4 to model bilayers consisting of 1,2-dioleoyl-*sn*-glycero-3-phosphocholine (DOPC) with or without cholesterol. In a bilayer with 30% cholesterol, the PLY monomer remained bound to the upper leaflet for the entire duration of the simulation (8 μs; Fig. 2*A* and *SI Appendix*, Fig. S1). By contrast, in the absence of cholesterol, we observed unbinding and dissociation of PLY from the membrane surface (after 0.5 μs; Fig. 2*B*). At higher cholesterol levels, the Trp-rich undecapeptide (residues Trp433, Trp435, and Trp436) along with L1 residues (Thr459, Leu460, Tyr461) interacted with cholesterol molecules directly but transiently (Fig. 2*C* and *SI Appendix*, Fig. S2). Peripheral membrane binding often triggers conformational changes in proteins (28). In the case of PLY, the undecapeptide residues Trp435 and Trp436 started out detached but then rearranged to anchor the protein into the bilayer (*SI Appendix*, Fig. S2). Hinge bending around D2 dominates the large-scale dynamics of the membrane-docked monomer (*SI Appendix*, Fig. S3). This motion has previously been associated with the transition of PLY to the so-called late prepore state (15, 19).

Coarse-grained MD simulations using the MARTINI model confirmed the docking sites and cholesterol dependence observed in atomistic MD simulations. PLY monomers docked spontaneously to the upper leaflet, using the undecapeptide and L1 residues (*SI Appendix*, Fig. S4). In simulations with mutations in undecapeptide and L1 residues, we observed fewer docking events and longer waiting times (*SI Appendix*, Fig. S5*A*). By contrast, cholesterol aided the docking of PLY to DOPC bilayers (*SI Appendix*, Fig. S5*B*). Despite its severely restricted backbone dynamics, the coarse-grained model thus captures key membrane interactions identified in our all-atom MD simulations.

Wetting and Lipid Depletion Near Pneumolysin. To test the impact of PLY on membrane structure, we performed all-atom MD simulations of PLY with membrane-inserted β-hairpins. In MD simulations of the monomer, we found that the transmembrane β-sheet formed by four antiparallel β-strands was strongly distorted, including the β-strands in D3. The high flexibility in D2 allowed D4 to tilt from an upright into a flatter position, loosening the contacts of L1 with the membrane. In one of two replicates, the β-sheet was completely pushed out of the membrane and PLY dislodged from the membrane (within 1 μs; *SI Appendix*, Fig. S6). In this process, first D1 and D3 were lifted. Once the tips of the β-hairpins lost contact with the polar head groups of the lipids, they quickly crossed the membrane. The tips of the bent β-sheet lay almost flat on the membrane. In oligomer simulations, we found that the outer β-strands of the transmembrane β-sheet of the PLY trimer (*SI Appendix*, Fig. S7) and of a PLY pentamer (Fig. 3) were also severely distorted into bent conformations. By contrast, the central β-strands of protomers in the pentamer were not distorted in a major way. Lateral cross-protomer H-bonds thus stabilize the β-sheet arcs upon insertion into the membrane (Fig. 3).

The transmembrane β-sheet formed by PLY oligomers in pore conformation has an outer hydrophobic face and an inner hydrophilic face, one attracting and the other repelling lipid tails. Within a few nanoseconds in the atomistic pentamer MD simulation, the inner face became hydrated. Water influx triggered lipid reorientation (Movie S1). Within 10 ns, the lipids facing the hydrophilic side of the β-sheets formed an open membrane edge with loosely packed lipids (Fig. 3*E*). The region between the edge and the β-sheet was devoid of lipids and allowed free exchange of water and ions across the membrane. In PLY-trimer simulations (*SI Appendix*, Fig. S7), distorted transmembrane arcs produce a narrow water channel. The zone of lipid clearance was more pronounced in the pentamer simulation (Fig. 3). The β-sheets of the pentamer arranged into

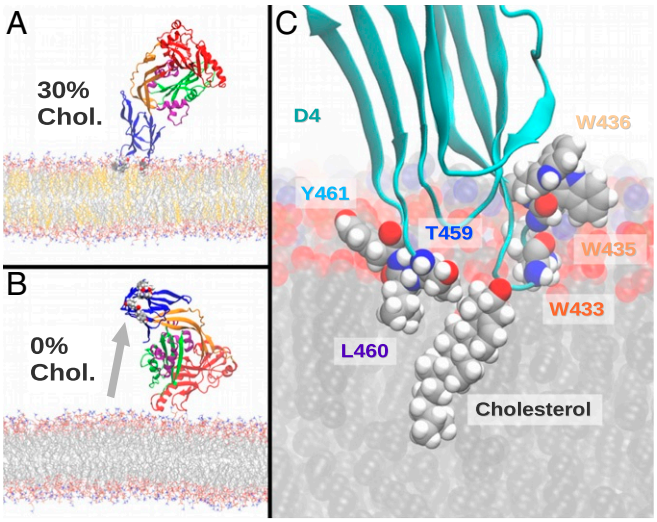

Fig. 2. Membrane interaction of PLY protomers. (*A* and *B*) Snapshots from all-atom MD simulations of PLY protomers that were initiated from structures docked to bilayers with and without cholesterol. (*C*) Zoom-in on membrane interaction in *A*, showing the Trp-rich undecapeptide and loop 1 in contact with a cholesterol molecule (highlighted spheres).

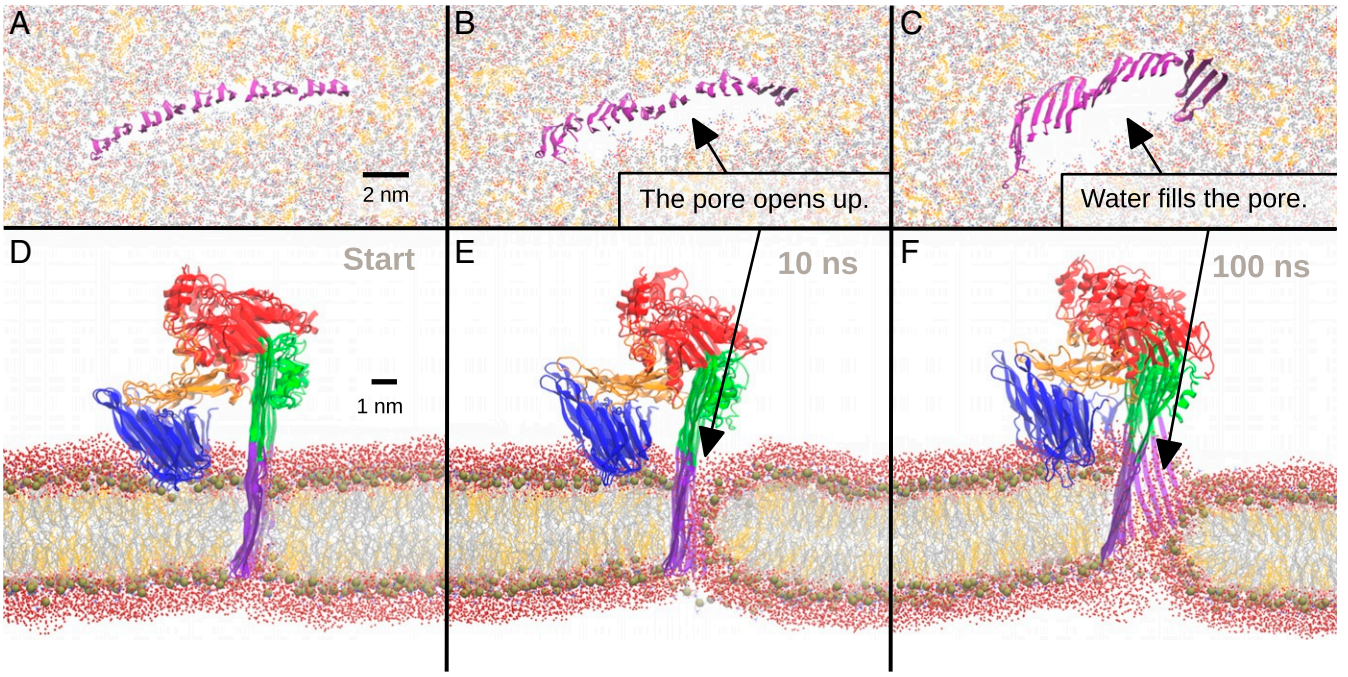

Fig. 3. Lipids recede from the hydrophilic inner surface of the transmembrane β-sheet formed by PLY oligomers in pore conformation. Shown are three snapshots from an all-atom MD simulation of an arc-shaped PLY pentamer embedded in a DOPC bilayer with 30% cholesterol, as seen from above (*A–C*) and along the transmembrane β-sheet (*D–F*). After water (red dots) is drawn to the inner face of the β-sheet (purple strands), the lipid molecules recede and form an open membrane edge that allows free exchange of lipids between the upper and lower leaflets (*B* and *E*). Water influx expands the gap into a membrane pore between the protein and the nascent bilayer edge. See *SI Appendix*, Figs. S6 and S7 for monomer and trimer simulations, respectively, and Movie S1.

a compact half-moon shape that remained stable throughout the following 1-μs simulation time with only one of the outer protomers being distorted (*SI Appendix*, Fig. S8*A*). The corresponding lipid fingerprint (29) shows that cholesterol preferably interacted with D4, whereas the lipid-adhered region on the outside of the inserted β-sheets was almost devoid of cholesterol, as was the free membrane edge (*SI Appendix*, Fig. S8 *B* and *C*). The inner face of the β-sheets preferentially interacted with cations (here, sodium; *SI Appendix*, Fig. S9) via a membrane-spanning region of acidic residues. While the monomer facilitated membrane entry and passage of only a few sodium ions (*SI Appendix*, Fig. S9 *A* and *B*), the trimer formed a persistent pore of about 2 nm diameter (*SI Appendix*, Fig. S9 *C* and *D*). The pentamer pore with its free membrane edge was already too large to be cation selective (*SI Appendix*, Fig. S9 *E* and *F*). These simulations provide an atomistically detailed view of the changes in membrane structure induced by fully inserted β-sheets and thus into the behavior of lipids, water, and ions during pore formation.

Lipid Escape from PLY Rings. To resolve the pore formation by complete PLY rings with 42 monomers, we performed MD simulations with the MARTINI coarse-grained model (30–32). We modeled different β-sheet insertion states as putative intermediates along a sequential insertion pathway, from a ring entirely in prepore conformation (0/42) to a fully inserted ring (42/42; Fig. 4 *A–F* and Movies S2–S4). In the MD simulations, the lipid tails quickly receded from the inner face of inserted β-sheet segments while water entered, and a membrane edge formed (Fig. 4 *A–F*), consistent with the observations from our atomistic simulations for small oligomers.

The enclosed membrane patches deformed to minimize the length of the exposed free edge. For all rings with more than 25% of the PLY β-hairpins inserted, we observed measurable changes in curvature of the enclosed bilayer patch (*SI Appendix*, Fig. S10). A small kink below adhered prepore protomers left the bilayer intact and continuous with the outside membrane (Fig. 4*G*, right). With all 42 protomers in pore conformation, the transmembrane β-sheet formed a cylindrical wall (Fig. 4 *F* and *J–L*). Lacking a connection to the outside membrane, the enclosed membrane patch detached from the hydrophilic wall and vesiculated (Fig. 4*F*).

Already in prepore conformation, fully formed PLY rings restrict the flow of lipids in and out of the ring. By tracing the motion of enclosed lipids, we found that the PLY undecapeptide and L1 in prepore conformation act as barriers for lipid diffusion in the upper leaflet. By contrast, lipids in the lower leaflet moved freely and mixed with the bulk (*SI Appendix*, Fig. S11). However, even though the lipids from the upper leaflet of the enclosed membrane patch could slide across the open edge and escape via the lower leaflet, this route is effectively blocked in our simulation setup. The reason is that such lipid efflux would build up pressure in the lower leaflet as a result of growing leaflet asymmetry. In effect, our setup traps the lipid plug (Fig. 4 *G–I*), allowing us to probe pore opening when β-sheet insertion is completed rapidly or when lipid efflux is hindered.

To overcome the restriction of lipid flow under periodic boundary conditions, we doubled the system size, simulating two equivalent rings adhered on opposite sides of the bilayer. The leaflet asymmetries built up by lipid efflux from the two rings exactly compensate, thus allowing the enclosed lipids to escape via the open edges (Fig. 4 *G–I* and *SI Appendix*, Figs. S11 and S13). The initially curved membrane plugs relaxed into a flatter configuration (*SI Appendix*, Fig. S10) as excess lipids drained out of the rings. In simulations of PLY rings with a greater fraction of protomers in pore conformation, the transmembrane β-hairpins restricted lateral lipid diffusion out of the ring and increased the relaxation times required for leaflet equilibration, leading to a slower decay of curvature of the enclosed bilayer patches (*SI Appendix*, Fig. S10).

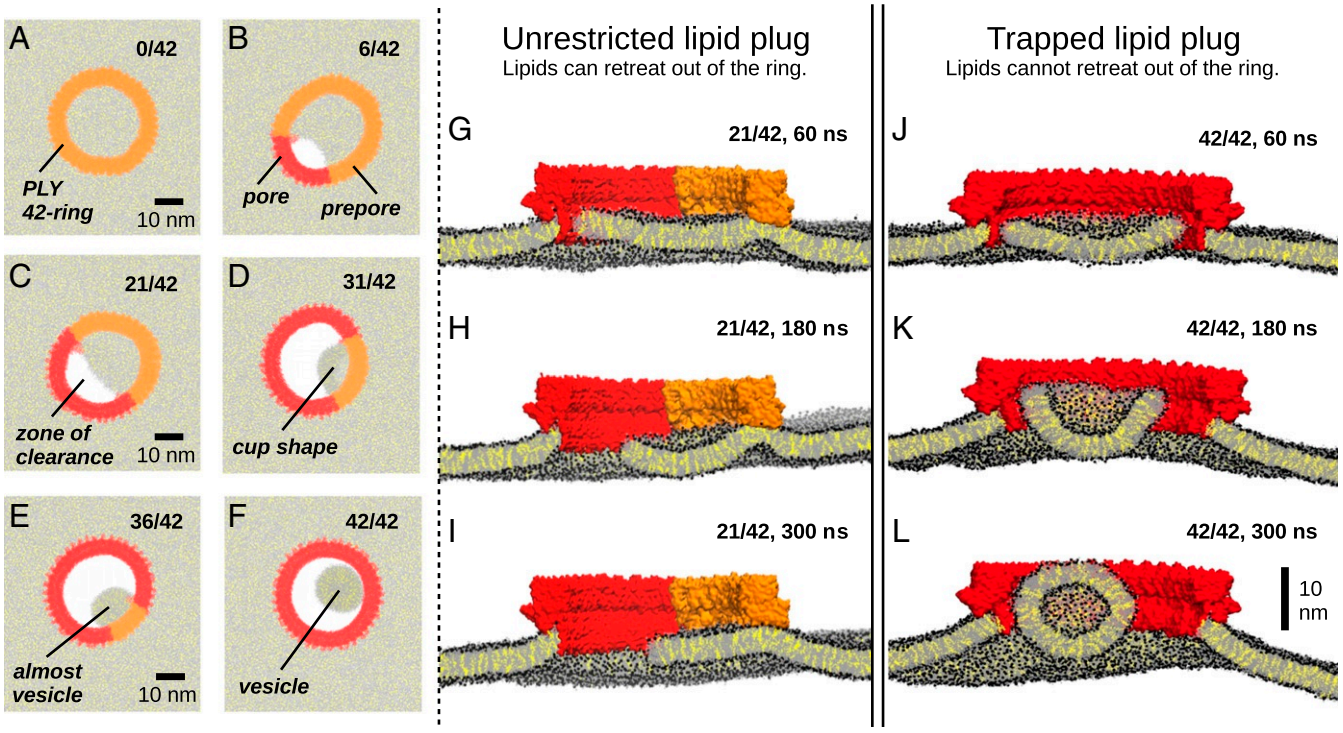

Fig. 4. Pore formation by pneumolysin. (*A–F*) Top views of final frames of independent coarse-grained simulations of PLY rings with increasing fraction of protomers in pore conformation (orange to red) inserted in DOPC bilayers (gray) with cholesterol (yellow). (*G–I*) Snapshots (cross-section) from simulation showing the effect of partial insertion (50% insertion, as in *C*) in a setup allowing free lipid flow out of the PLY ring via the lower leaflet. In this setup, the presence of an equivalent pore on the other leaflet (*SI Appendix*, Fig. S13) largely eliminates back pressure against lipid efflux. (*J–L*) Snapshots (cross-section) from simulation initiated from completely inserted PLY ring (red) as in *F*. The enclosed bilayer patch, constrained by the ring, forms a closed vesicle. In a cell, we expect that this vesicle will be expelled by osmotic flow, leaving a large cytolytic pore.

Validation by Experiment. The simulations make several concrete and testable predictions: Pore formation does not proceed to completion if not all protomers have inserted their helix bundles as β-hairpins, lipids attach to the prepore PLY segments in the ring, and the membrane buckles within pores that restrict lipid escape. In a survey of images from earlier AFM studies (15), we found several structures that closely resemble key intermediate configurations observed in our simulations (*SI Appendix*, Figs. S14–S16). In particular, we identified examples (*SI Appendix*, Fig. S14) for (*i*) complete prepores and (*ii*) complete pores. We also found (*iii*) a partially inserted ring with an arc of prepore conformations and an arc of pore conformations and (*iv*) a pore ring containing what appears to be a trapped lipid blob. The structures *iii* and *iv* are consistent with the simulation structures in Fig. 4 *H*, *I*, *K*, and *L*, respectively, as intermediate configurations with fractional insertions and a completely inserted ring with vesiculating lipids. The membrane deformations induced by the PLY ring are similar to those seen in recent cryo-EM experiments, both outside and inside the ring (10, 18, 19) (*SI Appendix*, Fig. S17).

Pore Opening by Vesiculation. Elastic theory (33) predicts that for small PLY ring radii, a fully detached membrane patch trapped inside a ring maintains an open-disk shape, whereas for large radii the line tension on the detached rim induces a spontaneous vesiculation of the patch. Using elastic theory (*SI Appendix*), we computed the energy for membrane shapes ranging from flat bilayer disks to spherical vesicles for a given PLY inner-ring radius R_0 (*SI Appendix*, Fig. S18). A similar transition occurs also for partially inserted pores (*SI Appendix*, Fig. S19). With values for the bending rigidity and line tension typical of plasma membranes, the transition between the two regimes occurs at $R_0 \approx 10$ nm, i.e., the typical size of PLY rings (10). Consistent with this estimate, prepore rings tend to have radii below R_0, and pore-conformation rings with open pores have larger radii, as seen in AFM and EM experiments (*SI Appendix*, Fig. S18*B*, *Bottom*).

Discussion

Simulations of PLY protomers docked to the membrane provided a detailed picture of membrane–protein interactions and cholesterol specificity. We found that Leu460/Thr459 of loop 1 and Trp433, Trp435, and Trp436 of the undecapeptide are the chief membrane-anchoring residues involved in cholesterol recognition and binding to the membrane, consistent with previous results (13–15, 34). In our simulations, Leu460/Thr459 interacted transiently but specifically with cholesterol molecules. These residues were previously found to be an important part of the cholesterol-recognition motif (16). Our atomistic simulations show in detail the interactions resulting in cholesterol specificity. Despite the limitations of the coarse-grained models imposed by the fixed protein geometry (24, 35), the coarse-grained simulations capture the cholesterol dependence of PLY membrane docking, a defining feature of the CDC family. Nevertheless, it is possible that cholesterol has additional stabilizing functions (36), as required for pore formation of alpha-toxins (37) or for dimerization of GPCRs (38).

The main principle behind PLY-induced pore formation is the rapid detachment of lipids from the hydrophilic inner face of the membrane-inserted β-barrel seen in both our atomistic and coarse-grained simulations. By contrast, the membrane at the hydrophobic outer face of the PLY ring remains intact. This behavior is a direct consequence of the distinct hydrophobicity pattern of opposite faces of the PLY ring (19). The

inserted β-strands have alternating hydrophobic and hydrophilic residues, resulting in a completely closed hydrophobic outer face and a hydrophilic inner face. The strong charge distribution along the β-hairpins shaping the inner surface draws in water and repels lipid acyl chains, resulting in lipid-depleted zones. The elastic network restraining secondary and tertiary structure of the coarse-grained model does not allow structural transitions to be modeled properly (24, 35) and the time scales of atomistic simulations are too short to observe prepore-to-pore transition. The exact process of insertion may thus deviate from our simulations that were initiated from the final pore conformation. Although we cannot simulate the complex conformational changes associated with helix-bundle unfolding, membrane insertion, and refolding as transmembrane β-hairpins, our simulations of the pore conformation provide a detailed view of the behavior of the enclosed lipids and water and of membrane pore formation from lipid detachment to plug release.

The main characteristics of the PLY pore structure were recognized in the initial cryo-EM model (19), refined here by molecular dynamics flexible fitting (MDFF) (39) (*Materials and Methods*) to maximize model/map correspondence. The closed barrel structure of the transmembrane β-sheet is a well-conserved feature of all CDCs. We expect the PLY system to provide us with a model for pore formation also for other CDCs, including the arc- or slit-like pores of LLO (40), which are reminiscent of what we saw here for small oligomers (Fig. 3). A similar mechanism of pore formation might be used by gasdermin-D, a related cytolytic protein involved in pyroptosis (41–44). Additionally, the formation of small cation-selective membrane pores in our PLY monomer and trimer simulations (*SI Appendix*, Fig. S9) hints at a possible mechanism for the selective ion permeability at sublytic PLY concentrations (11, 12). However, we cannot exclude that PLY at sublytic concentrations causes permeability by a different mechanism.

The last step in pore formation is the retraction of the segregated lipids, driven by minimizing the newly formed edge. The simulations of PLY protomers and oligomers suggest strong cooperativity in the insertion mechanism. Two scenarios for insertion of β-hairpins seem possible: (*i*) a single-step concerted process where all protomers of the ring insert their β-hairpins more or less simultaneously or (*ii*) a sequential step-by-step process, where protomers are inserted one after another, facilitated by the preceding insertion of a neighbor. AFM images of incomplete pores (15) (*SI Appendix*, Figs. S14–S16) and cryo-EM data (18) (*SI Appendix*, Fig. S17) show structures resembling intermediate configurations along a slow step-by-step insertion pathway or final stages of an imperfect concerted transition. Using large-scale simulations of fully formed rings, we examined the consequences of both scenarios.

If β-strand insertion is faster than lipid escape, the membrane plug remains trapped. For the typical size of PLY rings, $R_0 \approx 10$ nm, a closed vesicle forms spontaneously. By contrast, in a slow step-by-step insertion process, partial ring insertion allows the lipids to escape from the ring via the lower leaflet, unless hindered by other factors. Structures identified in our survey of AFM and cryo-EM images closely resemble key intermediates along both of these pathways.

It is conceivable that both pathways are exploited in *S. pneumoniae* infections. The large plasma membranes of mammalian cells can accommodate surplus lipids that move from one leaflet to the other within a partially inserted PLY pore. However, if lipid escape from the rings is constrained, the enclosed and partially detached membrane buckles. Lipid trapping and constrained diffusion also occur at a high surface density of PLY protomers (as observed in AFM (15) and cryo-EM (19) experiments), or in membrane regions separated by lipids immobilized through contacts with the cytoskeleton, or by different lipid composition (e.g., "rafts"). We showed that PLY is able to perforate the membrane also in this case by deforming the enclosed membrane patch. Membrane bending thus makes the process of pore opening insensitive to the surroundings of the ring in the target membrane.

Our elastic continuum model indicates that a minimum ring size is necessary for the bending and vesiculation of the enclosed lipid patch to proceed spontaneously. For cholesterol-containing membranes, we estimate a minimum inner pore radius of about 10 nm, corresponding to the most common size of PLY rings observed by cryo-EM (10) and AFM (15) (*SI Appendix*, Fig. S17*B*). Indeed, in experiment rings below this radius tended to maintain the prepore state, whereas larger rings transitioned to the pore form more frequently (15). Buckling of the membrane patch is an alternative pathway of pore opening, besides lipid efflux. Buckling overcomes the problem of lipid removal when β-sheet insertion is completed rapidly or when lipid efflux is hindered. The formation of large PLY rings may thus have offered an evolutionary advantage, for instance, to perforate sterol-containing membranes that are crowded with many PLY rings or corralled by interactions with the cytoskeleton.

In rings in which only a fraction of PLY protomers have inserted their hairpins, the lipid plug is still connected to the rest of the membrane and thus cannot leave completely. This problem arises also with other CDCs that do not form entire rings but arc- or slit-like pores. As our elastic model for partial insertion shows (*SI Appendix*, Fig. S19), membrane bending would facilitate the opening of a pore also in these cases.

Conclusions

We simulated PLY interactions with lipid membranes at atomistic and coarse-grained resolution and rationalized our findings by a continuum model of membrane free energy and comparison with experimental results. The membrane docking geometry proposed from experiments was confirmed (16). Key amino acids are buried in the membrane, forming transient interactions with cholesterol to stabilize toxin binding.

The transition of the prepore to the pore state requires a high degree of cooperativity. Expulsion of lipids from the hydrophilic inner rim of the inserted pore is identified as the key principle of cytolytic activity. For both concerted and sequential insertion, membrane bending aids the formation of a pore when the lipids cannot easily escape from the ring enclosure. Membrane elastic theory implies that this bending process occurs spontaneously only for rings with a radius larger than about 10 nm for typical cholesterol-containing membranes. PLY and other CDC pores may thus have evolved to larger sizes compared with other classes of PFTs to perforate also membranes that contain cholesterol and that are corralled by interactions with the cytoskeleton to prevent easy lateral escape of lipid plugs.

Supporting Information. Supporting information (SI) contains *SI Appendix*, Figs. S1–S22, Tables S1–S6, and *SI Text* along with Movies S1–S4.

Materials and Methods

The crystal structure of pneumolysin (PDB code: 5CR6) (13) served as a model of the early prepore conformation (15) in our simulations of membrane–protein interactions. For the pore conformation, we started from the cryo-EM structure (PDB code: 5LY6) (19) and refined it using MDFF (39). The atomistic simulations of PLY monomers and multimers at and in DOPC membranes with 30% cholesterol used the CHARMM36m force field (45). Systems were set up with the help of the CHARMM-GUI membrane builder (46). The coarse-grained simulations of PLY docking and PLY rings were performed in Gromacs 5 (47) using the MARTINI model (v2.2) for lipids (31) and its extension to proteins (32). Coarse-grained models of pneumolysin

protomers and rings were generated from their all-atom models using martinize.py version 2.6 (48). Harmonic restraints on backbone beads were imposed using an elastic network model (ElNeDyn) (35). See *SI Appendix* for details.

ACKNOWLEDGMENTS. We thank Jürgen Köfinger, Lukas Stelzl, Alfredo Jost López, and Michael Gecht for helpful discussions. We also thank Matthew Leipner for help with the analysis of the AFM data. This work was supported by the Max Planck Society.

1. A. M. Berry, J. Yother, D. E. Briles, D. Hansman, J. C. Paton, Reduced virulence of a defined pneumolysin-negative mutant of Streptococcus pneumoniae. *Infect. Immun.* **57**, 2037–2042 (1989).
2. J. E. Alouf, Molecular features of the cytolytic pore-forming bacterial protein toxins. *Folia Microbiol.* **48**, 5–16 (2003).
3. R. K. Tweten, Cholesterol-dependent cytolysins, a family of versatile pore-forming toxins. *Infect. Immun.* **73**, 6199–6209 (2005).
4. R. J. Gilbert, Inactivation and activity of cholesterol-dependent cytolysins: What structural studies tell us. *Structure* **13**, 1097–1106 (2005).
5. R. Ramachandran, R. K. Tweten, A. E. Johnson, Membrane-dependent conformational changes initiate cholesterol-dependent cytolysin oligomerization and intersubunit β-strand alignment. *Nat. Struct. Mol. Biol.* **11**, 697–705 (2004).
6. S. Bhakdi *et al.*, A guide to the use of pore-forming toxins for controlled permeabilization of cell membranes. *Med. Microbiol. Immunol.* **182**, 167–175 (1993).
7. R. K. Tweten, M. W. Parker, A. E. Johnson, The cholesterol-dependent cytolysins. *Curr. Top. Microbiol. Immunol.* **257**, 15–33 (2001).
8. A. Olofsson, H. Hebert, M. Thelestam, The projection structure of Perfringolysin-O (Clostridium-perfringens Omicron-toxin). *FEBS Lett.* **319**, 125–127 (1993).
9. O. Shatursky *et al.*, The mechanism of membrane insertion for a cholesterol-dependent cytolysin: A novel paradigm for pore-forming toxins. *Cell* **99**, 293–299 (1999).
10. S. J. Tilley, E. V. Orlova, R. J. C. Gilbert, P. W. Andrew, H. R. Saibil, Structural basis of pore formation by the bacterial toxin pneumolysin. *Cell* **121**, 247–256 (2005).
11. Y. E. Korchev, C. L. Bashford, C. A. Pasternak, Differential sensitivity of pneumolysin-induced channels to gating by divalent cations. *J. Membr. Biol.* **127**, 195–203 (1992).
12. J. S. Braun, J. E. Sublett, J. R. Weber, Pneumococcal pneumolysin and H_2O_2 mediate brain cell apoptosis during meningitis. *J. Clin. Invest.* **109**, 19–27 (2002).
13. J. E. Marshall *et al.*, The crystal structure of pneumolysin at 2.0 Å resolution reveals the molecular packing of the pre-pore complex. *Sci. Rep.* **5**, 13293 (2015).
14. S. L. Lawrence *et al.*, Crystal structure of Streptococcus pneumoniae pneumolysin provides key insights into early steps of pore formation. *Sci. Rep.* **5**, 14352 (2015).
15. K. Van Pee, E. Mulvihill, D. J. Müller, Ö. Yildiz, Unraveling the pore-forming steps of pneumolysin from Streptococcus pneumoniae. *Nano Lett.* **16**, 7915–7924 (2016).
16. A. J. Farrand, S. LaChapelle, E. M. Hotze, A. E. Johnson, R. K. Tweten, Only two amino acids are essential for cytolytic toxin recognition of cholesterol at the membrane surface. *Proc. Natl. Acad. Sci. U.S.A.* **107**, 4341–4346 (2010).
17. S. Köster *et al.*, Crystal structure of listeriolysin O reveals molecular details of oligomerization and pore formation. *Nat. Commun.* **5**, 3690 (2014).
18. A. F. Sonnen, J. M. Plitzko, R. J. Gilbert, Incomplete pneumolysin oligomers form membrane pores. *Open Biol.* **4**, 140044 (2014).
19. K. van Pee *et al.*, CryoEM structures of membrane pore and prepore complex reveal cytolytic mechanism of pneumolysin. *eLife* **6**, 1–22 (2017).
20. D. Stoddart *et al.*, Functional truncated membrane pores. *Proc. Natl. Acad. Sci. U.S.A.* **111**, 2425–2430 (2014).
21. N. Jia *et al.*, Structural basis for receptor recognition and pore formation of a zebrafish aerolysin-like protein. *EMBO Rep.* **17**, 235–248 (2016).
22. C. Gatsogiannis *et al.*, Membrane insertion of a Tc toxin in near-atomic detail. *Nat. Struct. Mol. Biol.* **23**, 884–890 (2016).
23. N. Cirauqui, L. A. Abriata, F. G. Van Der Goot, M. Dal Peraro, Structural, physicochemical and dynamic features conserved within the aerolysin pore-forming toxin family. *Sci. Rep.* **7**, 1–12 (2017).
24. R. Desikan, S. M. Patra, K. Sarthak, P. K. Maiti, K. G. Ayappa, Comparison of coarse-grained (MARTINI) and atomistic molecular dynamics simulations of α and β toxin nanopores in lipid membranes. *J. Chem. Sci.* **129**, 1017–1030 (2017).
25. R. Desikan, P. K. Maiti, K. G. Ayappa, Assessing the structure and stability of transmembrane oligomeric intermediates of an α-helical toxin. *Langmuir* **33**, 11496–11510 (2017).
26. M. S. Vaidyanathan, P. Sathyanarayana, P. K. Maiti, S. S. Visweswariah, K. G. Ayappa, Lysis dynamics and membrane oligomerization pathways for Cytolysin A (ClyA) pore-forming toxin. *RSC Adv.* **4**, 4930–4942 (2014).
27. A. A. Lee, M. J. Senior, M. I. Wallace, T. E. Woolley, I. M. Griffiths, Dissecting the self-assembly kinetics of multimeric pore-forming toxins. *J. R. Soc. Interf.* **13**, 20150762 (2016).
28. D. P. Hoogerheide *et al.*, Structural features and lipid binding domain of tubulin on biomimetic mitochondrial membranes. *Proc. Natl. Acad. Sci. U.S.A.* **114**, E3622–E3631 (2017).
29. V. Corradi *et al.*, Lipid-protein interactions are unique fingerprints for membrane proteins. *ACS Cent. Sci.* **4**, 709–717 (2018).
30. S. J. Marrink, H. J. Risselada, S. Yefimov, D. P. Tieleman, A. H. D. Vries, The MARTINI force field: Coarse grained model for biomolecular simulations. *J. Phys. Chem. B* **111**, 7812–7824 (2007).
31. S. J. Marrink, D. P. Tieleman, Perspective on the MARTINI model. *Chem. Soc. Rev.* **42**, 6801–6822 (2013).
32. L. Monticelli *et al.*, The MARTINI coarse-grained force field: Extension to proteins. *J. Chem. Theory. Comput.* **4**, 819–834 (2008).
33. W. Helfrich, Elastic properties of lipid bilayers: Theory and possible experiments. *Z. Naturforsch C* **28**, 693–703 (1973).
34. C. E. Soltani, E. M. Hotze, A. E. Johnson, R. K. Tweten, Structural elements of the cholesterol-dependent cytolysins that are responsible for their cholesterol-sensitive membrane interactions. *Proc. Natl. Acad. Sci. U.S.A.* **104**, 20226–20231 (2007).
35. X. Periole, M. Cavalli, S. J. Marrink, M. A. Ceruso, Combining an elastic network with a coarse-grained molecular force field: Structure, dynamics, and intermolecular recognition. *J. Chem. Theory Comput.* **5**, 2531–2543 (2009).
36. K. S. Giddings, A. E. Johnson, R. K. Tweten, Redefining cholesterol's role in the mechanism of the cholesterol-dependent cytolysins. *Proc. Natl. Acad. Sci. U.S.A.* **100**, 11315–11320 (2003).
37. P. Sathyanarayana *et al.*, Cholesterol promotes cytolysin A activity by stabilizing the intermediates during pore formation. *Proc. Natl. Acad. Sci. U.S.A.* **115**, E7323–E7330 (2018).
38. K. Pluhackova, S. Gahbauer, F. Kranz, T. A. Wassenaar, R. A. Böckmann, Dynamic cholesterol-conditioned dimerization of the G protein coupled chemokine receptor type 4. *PLoS Comput. Biol.* **12**, 1–25 (2016).
39. L. G. Trabuco, E. Villa, E. Schreiner, C. B. Harrison, K. Schulten, Molecular dynamics flexible fitting: A practical guide to combine cryo-electron microscopy and X-ray crystallography. *Methods* **49**, 174–180 (2009).
40. E. Mulvihill, K. Van Pee, S. A. Mari, D. J. Müller, Ö Yildiz, Directly observing the lipid-dependent self-assembly and pore-forming mechanism of the cytolytic toxin listeriolysin O. *Nano Lett.* **15**, 6965–6973 (2015).
41. J. Shi *et al.*, Cleavage of GSDMD by inflammatory caspases determines pyroptotic cell death. *Nature* **526**, 660–665 (2015).
42. L. Sborgi *et al.*, GSDMD membrane pore formation constitutes the mechanism of pyroptotic cell death. *EMBO J.* **35**, 1766–1778 (2016).
43. J. Ding *et al.*, Pore-forming activity and structural autoinhibition of the gasdermin family. *Nature* **535**, 111–116 (2016).
44. E. Mulvihill *et al.*, Mechanism of membrane pore formation by human gasdermin-D. *EMBO J.* **37**, e98321 (2018).
45. J. Huang *et al.*, CHARMM36m: An improved force field for folded and intrinsically disordered proteins. *Nat. Methods* **14**, 71–73 (2016).
46. J. Lee *et al.*, CHARMM-GUI input generator for NAMD, GROMACS, AMBER, OpenMM, and CHARMM/OpenMM simulations using the CHARMM36 additive force field. *J. Chem. Theory Comput.* **12**, 405–413 (2016).
47. M. J. Abraham *et al.*, Gromacs: High performance molecular simulations through multi-level parallelism from laptops to supercomputers. *SoftwareX* **1-2**, 19–25 (2015).
48. D. H. De Jong *et al.*, Improved parameters for the MARTINI coarse-grained protein force field. *J. Chem. Theory Comput.* **9**, 687–697 (2013).